GDCh

Research Articles

Angewandte
Chemie
International Edition
www.angewandte.org

Photoelectrochemical H₂O splitting

Subsurface Engineering Induced Fermi Level De-pinning in Metal Oxide Semiconductors for Photoelectrochemical Water Splitting

Jun Wang, Ganghai Ni, Wanru Liao, Kang Liu, Jiawei Chen, Fangyang Liu,
Zongliang Zhang, Ming Jia, Jie Li, Junwei Fu, Evangelina Pensa, Liangxing Jiang,*
Zhenfeng Bian,* Emiliano Cortés,* and Min Liu*

Abstract: Photoelectrochemical (PEC) water splitting is a promising approach for renewable solar light conversion. However, surface Fermi level pinning (FLP), caused by surface trap states, severely restricts the PEC activities. Theoretical calculations indicate subsurface oxygen vacancy (sub-O_v) could release the FLP and retain the active structure. A series of metal oxide semiconductors with sub-O_v were prepared through precisely regulated spin-coating and calcination. Etching X-ray photoelectron spectroscopy (XPS), scanning transmission electron microscopy (STEM), and electron energy loss spectra (EELS) demonstrated O_v located at sub ~2–5 nm region. Mott–Schottky and open circuit photovoltage results confirmed the surface trap states elimination and Fermi level de-pinning. Thus, superior PEC performances of 5.1, 3.4, and 2.1 mA cm^{-2} at 1.23 V vs. RHE were achieved on $BiVO_4$, Bi_2O_3, TiO_2 with outstanding stability for 72 h, outperforming most reported works under the identical conditions.

Introduction

The environmental-friendly photoelectrochemical (PEC) water splitting opens up a new avenue for the conversion of renewable solar light into green hydrogen energy.[1] Oxide semiconductors, acting as the most promising photoanodes, have attracted considerable attention as their advantages of facile preparation, abundant resources, and excellent photochemical stability.[2] In PEC system, the Fermi level (E_F) of photoanode needs to equilibrate with the redox potential (E_{redox}) of the electrolyte (Figure S1). However, abundant intrinsic surface trap states cause significant potential drop within the Helmholtz layer, resulting the so-called "Fermi level pinning (FLP)" effect (Figure 1) and reduced open circuit photovoltage (V_{ph}) driving force for PEC water oxidation under illumination.[3]

Tremendous strategies have been developed to overcome the FLP effect. For instance, oxygen or ultraviolet-ozone treatment can effectively eliminate the oxygen vacancy (O_v) trap states.[4] While, the positive roles of charge separation and catalytic sites on these surface states would also be destroyed.[5] Heteroatoms doping could adjust the work function of semiconductor to release FLP effect, yet the accompanied lattice damage limits its further application.[6] Recently, ultrathin amorphous layer (Al_2O_3, TiO_2, and ZnO etc.) was used to passivate the surface trap states.[7] The suppressed FLP effect could greatly reduce the overpotential required to photooxidize water, but most of them rely on expensive and time-consuming atomic layer deposition routes.[8]

As an alternative approach, constructing subsurface oxygen vacancy (sub-O_v) located at ~2–10 nm region below the outermost layer is proved favorable for increasing

---

[*] Dr. J. Wang, J. Chen, Prof. F. Liu, Prof. Z. Zhang, Prof. M. Jia,
 Prof. J. Li, Prof. L. Jiang
 School of Metallurgy and Environment, Central South University
 Changsha 410083, Hunan (P.R. China)
 E-mail: lxjiang@csu.edu.cn

 Dr. J. Wang, G. Ni, Dr. W. Liao, Dr. K. Liu, Prof. J. Fu, Prof. M. Liu
 Hunan Joint International Research Center for Carbon Dioxide
 Resource Utilization, State Key Laboratory of Powder Metallurgy,
 School of Physics and Electronics, Central South University
 Changsha 410083, Hunan (P.R. China)
 E-mail: minliu@csu.edu.cn

 Prof. L. Jiang
 Hunan Provincial Key Laboratory of Nonferrous Value-added Metal-
 lurgy
 Changsha 410083, Hunan (P.R. China)

 Prof. Z. Bian
 MOE Key Laboratory of Resource Chemistry and Shanghai Key
 Laboratory of Rare Earth Functional Materials, Shanghai Normal
 University
 Shanghai 200234 (P.R. China)
 E-mail: bianzhenfeng@shnu.edu.cn

 Dr. E. Pensa, Prof. E. Cortés
 Nanoinstitut München, Fakultät für Physik, Ludwig-Maximilians-
 Universität München
 80539 München (Germany)
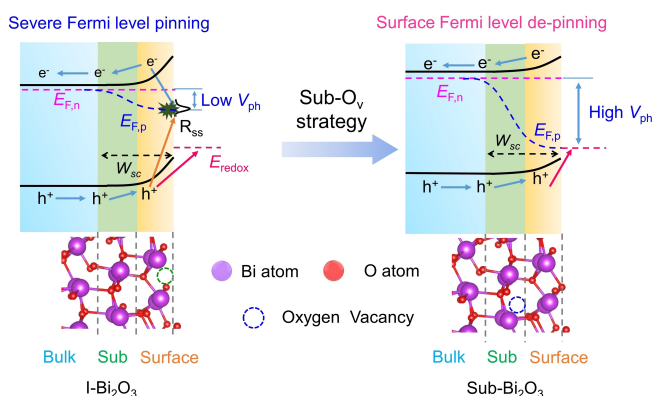 E-mail: Emiliano.Cortes@lmu.de

Figure 1. Schematic diagram of sub-O_v strategy for Fermi level de-pinning. V_{ph}, open-circuit photovoltage; $E_{F,n}$ and $E_{F,p}$, quasi-Fermi level of electrons and holes, respectively; R_{ss}, surface trap state recombination; E_{redox}, redox potential of electrolyte; W_{sc}, depletion layer width. Bi_2O_3 slab is utilized as the prototype to demonstrate the release of the severe FLP effect by introducing O_v in the subsurface region.

carrier concentration and exposing catalytic sites.[9] Meanwhile, the ordered outmost surface atomic arrangement displays the potential as the self-passivation layer to simultaneously eliminate the surface trap states and retain the active O_v structures.

Herein, we developed a universal sub-O_v strategy to alleviate the severe surface FLP for efficient water splitting. Through theoretical calculations and experimental results, O_v at the sub $\sim$2–5 nm region below the outermost layer could effectively remove the surface trap states to achieve

Fermi level de-pinning, leading to increased V_{ph} and boosted carrier transfer. Meanwhile, sub-O_v effectively promotes catalytic kinetics. Consequently, outstanding activities of 5.1, 3.4, and 2.1 mA cm^{-2} at 1.23 V vs. RHE for over 72 h are achieved on typical $BiVO_4$, Bi_2O_3, and TiO_2 respectively in Na_2SO_4 solution without scavengers, far exceeding most reported works. This sub-O_v strategy identifies a new inspiration for activating and boosting the performance of metal oxide semiconductors in photoelectrochemistry.

Results and Discussion

Bi_2O_3 is utilized as the prototype for investigating sub-O_v induced Fermi level de-pinning, due to its lower Bi–O bond energy and well-dispersed valence bands by the hybridization of Bi 6s and O 2p orbits.[10] Density functional theory (DFT) calculations were first conducted by using Bi_2O_3 slab with different types of O_v (Figure S2, inherent Bi_2O_3 with surface oxygen vacancy named I–Bi_2O_3; modified Bi_2O_3 with sub-O_v named Sub–Bi_2O_3; and traditional passivated Bi_2O_3 with no vacancy named P–Bi_2O_3). Clearly, the intrinsic surface oxygen vacancy (s-O_v) of I–Bi_2O_3 generates a shallow trap state near the conduction band minimum (CBM) (Figure 2a).[11] Through partial charge density distribution analysis, this localized state is contributed by the outermost surface Bi and O atoms (Figure 2d and Figure S3b), and the abundant surface trap states tend to pin the quasi-Fermi level of photo-generated holes,[12] leading to serious surface FLP within PEC water splitting process.
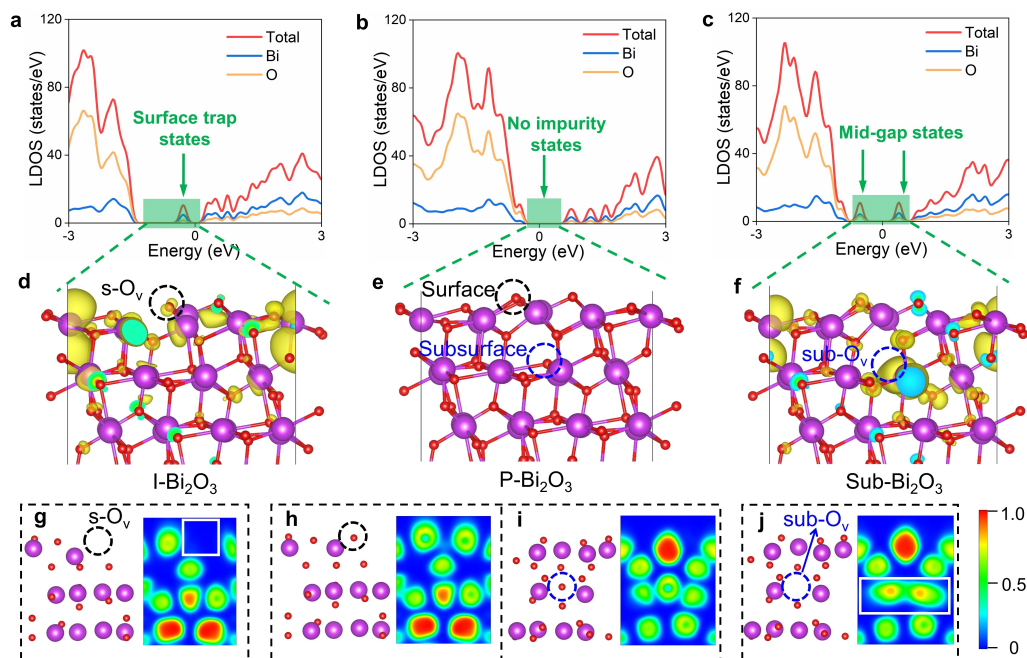

Figure 2. Theoretical prediction of sub-O_v induced Fermi level de-pinning. Calculated local density of states (LDOS) of a) I–Bi_2O_3, b) P–Bi_2O_3, and c) Sub–Bi_2O_3 slabs. Partial charge densities of the mid-gap states for d) I–Bi_2O_3, e) P–Bi_2O_3, and f) Sub–Bi_2O_3. Optimized cell structures and the corresponding charge density mapping of g) I–Bi_2O_3, h), i) P–Bi_2O_3, and j) Sub–Bi_2O_3, in which (h) and (i) are the results of P–Bi_2O_3 at different view-sections. In panels (d)−(f), the atomic contribution to the density of states is included in yellow.

The elimination of O_v can completely passivate the surface trap states to suppress the FLP effect (Figure 2b, Figure 2e, and Figure S3a), since no impurity states emerge within the band gap. While, the negatively shifted E_F away from CBM to valance band maximum (VBM) endows the transformation of the n-type I–Bi_2O_3 to p-type semiconductor (P–Bi_2O_3), significantly weakens the anodic current response. Interestingly, the Sub–Bi_2O_3 still remains typical n-type semiconductor property (Figure 2c). Although the introduction of O_v at subsurface area creates mid-gap states close to the CBM and VBM, the charge densities of the emerged impurity states arise primarily from the subsurface atoms (Figure 2f and Figure S3c). On this condition, outermost surface atoms make little contribution to mid-gap states, which sharply alleviate surface trap states to de-pin Fermi level.

From the crystal structure and partial charge density mapping results (Figures 2g–j), the presence of sub-O_v brings slight distortion to neighboring atoms and leads to obvious electron localization. Specifically, the neighboring Bi and O atoms show considerable charge accumulation and more overlap areas of electron wavefunction, which is in favor of the charge separation to participate the water splitting process along the defective conducting channels (Figure 2j).[13] On the contrary, s-O_v acts as the surface recombination center for quenching the photo-induced carriers (Figure 2g). These results reveal that sub-O_v exhibits potential for Fermi level de-pinning with retaining active O_v structures.

Through facile sol-gel based spin coating method, Bi_2O_3 samples were synthesized on WO_3/FTO substrate (Figure 3a and Figures S4–6).[14] For the XRD patterns of the as-prepared samples (Figure S7), the characteristic peak at 27.9° can be ascribed to the (201) plane of tetragonal Bi_2O_3 (β-Bi_2O_3). Raman spectra and electron spin resonance (ESR) were carried out to probe the oxygen defect structure. Clearly, the characteristic bands at around 600 cm^{-1} of I–Bi_2O_3 and Sub–Bi_2O_3 corresponded to the presence of O_v (Figure S8).[15] Meanwhile, typical signals at g = 2.003 can be identified as the single electron trapped O_v (Figure S9).[16] In contrast, no paramagnetic signal at g = 2.003 and Raman shift at 600 cm^{-1} were observed on P–Bi_2O_3 after the treatment in oxygen-rich environment, manifesting the complete elimination of single electron trapped O_v structure.

To verify the accurate constructing of sub-O_v, geometric local fine structures of the samples were characterized using aberration-corrected high-angle annular dark-field scanning transmission electron microscopy (HAADF-STEM) and electron energy-loss spectroscopy (EELS). In order to observe O_v induced lattice distortion phenomena more intuitively, inverse fast fourier transform (IFFT) process of the samples are carried out (Figures S10–S12).[17] Obvious lattice disorder can be observed within surface region of I–Bi_2O_3, which can be ascribed to the inherent O_v (Figure 3c and Figure S10). The interlayer spacing of 0.319 nm corresponds to the (201) diffraction plane of β-Bi_2O_3. In comparison, the O_v is eliminated and the atomic arrangement becomes ordered in P–Bi_2O_3 (Figure 3b and Fig-

ure S11). The unique migration feature of oxygen vacancy from the top layer to the subsurface in a series of oxide semiconductors have been proved in the previous works.[18] Under appropriate annealing condition, the lattice oxygen in the subsurface region will migrate to the surface area, fill the intrinsic s-O_v to form the sub-O_v. For Sub–Bi_2O_3 sample under optimized annealing condition, lattice distortion with the included angles around 6° appears at the sub ~2–5 nm region below outermost layer (Figure 3d and Figure S12), which can be attributed to the presence of sub-O_v. In the EELS O K-edge spectra, the intensity ratio of the pre-peak a to b (a/b) was used to evaluate the local oxygen content at different regions (Figure 3e, Figure S13, and Table S1).[19] Compared with outermost surface (0.915) and interior bulk (0.97) areas, the decrease of the a/b ratio (0.669) at sub ~2–5 nm reveals the presence of O_v at subsurface region.

For further validating the generation of sub-O_v, argon-ion-cluster etching-XPS experiments were conducted, as the gas ion cluster beam with lower energy significantly suppress the surface structure damage.[20] The spectra were collected at each etching step length of 1 nm (total of 7 nm from outermost surface inward) (Figures 3f–i and Figures S14–15). Prior to etching (0 nm), compared with stoichiometric Bi_2O_3, the peak of lattice oxygen shifts positively from 529.9 eV to 530.2 eV in Sub–Bi_2O_3. Meanwhile, the symmetric Bi $4f$ peaks at 162.46 eV and 157.15 eV are assigned to unsaturated coordinated $Bi^{\delta+}$ ($0 < \delta < 3$) species, reveals the presence of O_v in outer layer.

With the increased etching depth to 2 nm, little difference can be observed on the intensity and binding energy of $Bi^{\delta+}$ and lattice oxygen (Figures 3f-g). Meanwhile, the unobserved peak at approximately 531.1 eV (which belongs to surface chemisorbed oxygen species at O_v sites) certifies the non-existence of O_v in ordered outermost ~2 nm area.[21] Continuing etching inward from 3 to 6 nm, the signals of $Bi^{\delta+}$ decrease gradually and finally disappear at the depth of 6 nm for Sub–Bi_2O_3. Notably, the characteristic O_v peak at 531.2 eV only emerge within 3–5 nm etching depth region (Figure 3g and i). On the contrary, the concentration profile of low valence $Bi^{\delta+}$ species and O_v show different variation laws as a function of etching depth in I–Bi_2O_3 and P–Bi_2O_3 counterparts, respectively (Figure 3h and i, see detailed discussion in Figures S14– S15). These results indicate that O_v and the corresponding low valence Bi species only exist within the subsurface ~2–5 nm region, demonstrating the successful synthesis of Sub–Bi_2O_3.

Attributed to the construction of sub-O_v, Sub–Bi_2O_3 exhibits a sharply lowered photoluminescence (PL) intensity, illustrating fastest intrinsic photo-carrier separation of sub–Bi_2O_3 (Figure 4a). The average carrier lifetime ($\tau_{average}$) of Sub–Bi_2O_3 (29.04 ns) is about twice that of P–Bi_2O_3 (13.47 ns) and I–Bi_2O_3 (17.36 ns). The extended $\tau_{average}$ can be put down to the passivated surface trap states through sub-O_v construction, leading to reduced radiative recombination of the photo-generated carriers (Figure 4b).

The dependence of the flat band potential (E_{fb}) on the solution pH value was then carried out (Figure 4c and Figures S16–S18) to demonstrate the Fermi level de-pinning by sub-O_v. Ideally, the E_{fb} value and pH value will change
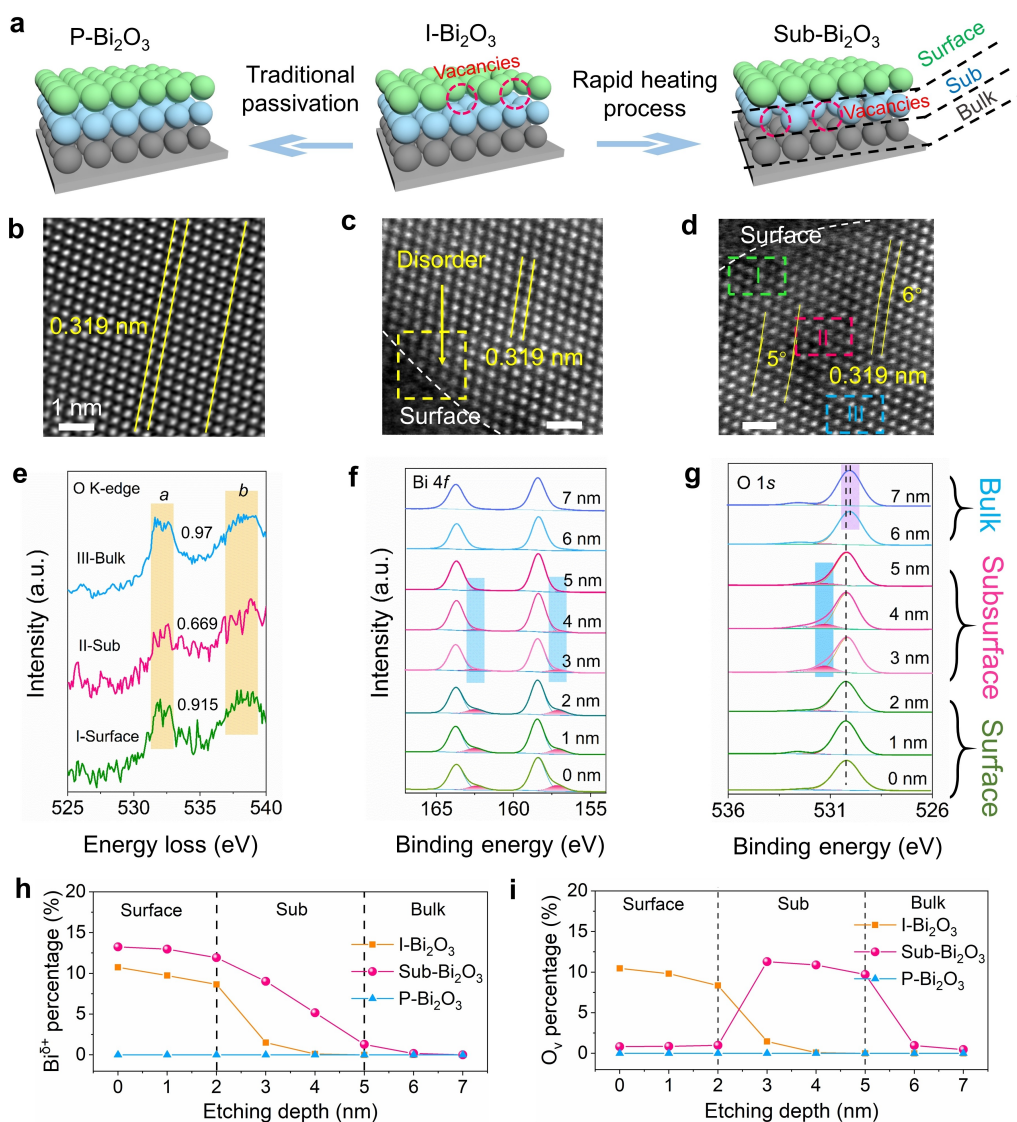
Figure 3. Material characterization. a) Schematic diagram for the fabrication of the photoanodes. Aberration-corrected high-angle annular dark-field scanning transmission electron microscopy (HAADF-STEM) images of b) P–Bi_2O_3, c) I–Bi_2O_3, and d) Sub–Bi_2O_3. e) EELS O K-edge spectra of Sub–Bi_2O_3 at different regions (I for surface, II for subsurface, and III for bulk areas, respectively). In situ etching-XPS spectra of f) Bi $4f$ and g) O 1s orbits for Sub–Bi_2O_3 with the etching depth from 0 to 7 nm. Concentration profile of h) low valence $Bi^{\delta+}$ species and i) characteristic O_v as a function of etching depth for different samples.

by $-59\,mV\,pH^{-1}$ for oxide semiconductors.[22] I–Bi_2O_3 gives rise to the slope of $-47\,mV\,pH^{-1}$, which can be ascribed to the surface FLP effect (Table S2). The reduced V_{ph} and corresponding slower photovoltage decay further confirmed the photo-induced electrons are easily captured by the surface trap states (Figure 4d). It is worth note that Sub–Bi_2O_3 exhibits an identical slope of $-58.3\,mV\,pH^{-1}$ to that of P–Bi_2O_3, suggesting a near ideal Fermi level de-pinning through sub-O_v construction (Figure 4c).[23] Since the depletion layer width of as-prepared samples are about 5 nm (see details in Table S3), sub-O_v can directly regulate the band bending degree under illumination (Figure 1). A higher V_{ph} value of 0.633 V is achieved on Sub–Bi_2O_3, providing a more beneficial driving force for water oxidation since it determines the difference between hole quasi-Fermi level and the redox potential of electrolyte.[6] The rapid photovoltage decay implies the sub-O_v could dramatically deactivate the surface trap and reduce the loss of holes via instant electron-hole recombination.[24] Besides, the significant decrease in the onset potential (E_{onset}) from 0.525 V (I–Bi_2O_3) to 0.406 V (Sub–Bi_2O_3) is attributed to the larger V_{ph} provided by the Fermi level de-pinning (Figure 4e).

Photoelectrochemical impedance spectroscopy (PEIS) incisively illustrate the catalytic kinetics under illumination. Typical Nyquist plot of Sub–Bi_2O_3 at 1.23 V vs. RHE exhibits the smallest radius of the semicircle curve at low-frequency region. By fitting the data with a typical two-RC-unit equivalent circuit model, the trapping resistance ($R_{ct, trap}$) of Sub–Bi_2O_3 is much lower than those of I–Bi_2O_3 and P–Bi_2O_3, suggesting the accelerated charge transfer at
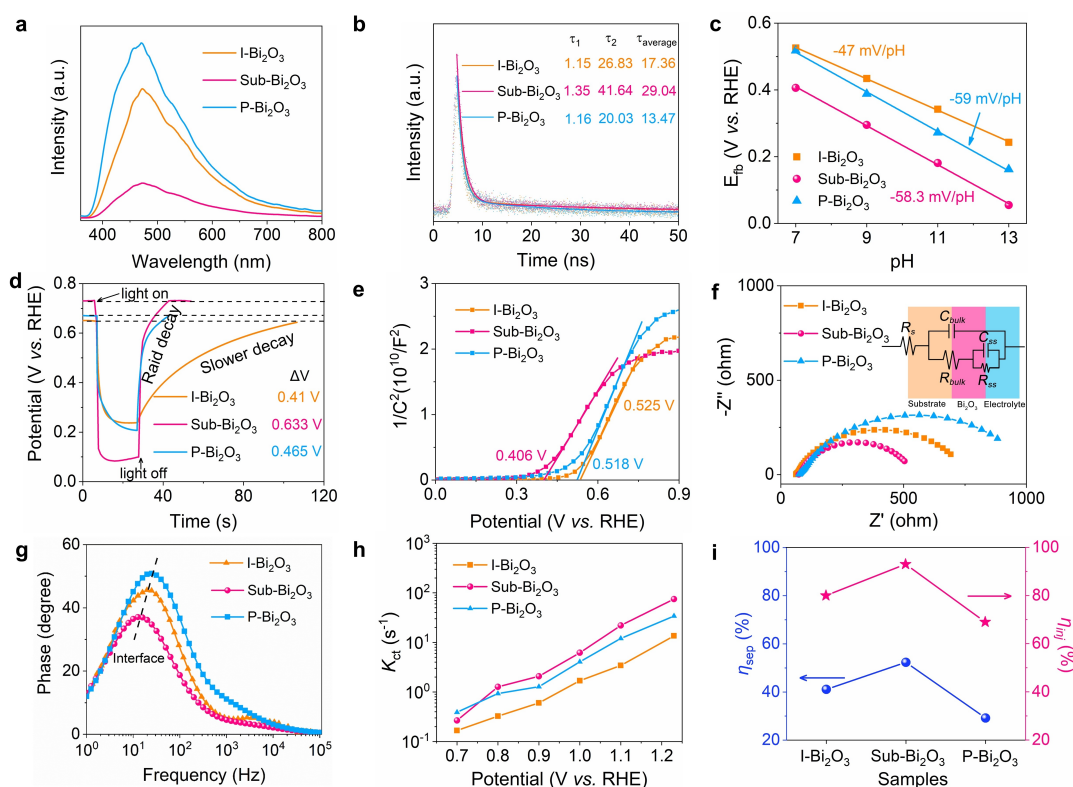
Figure 4. Fermi level de-pinning induced accelerated charge transfer. a) Photoluminescence spectra, and b) Time-resolved photoluminescence spectra of as-prepared samples. c) Dependence of the flat band potential (E_{fb}) on the solution pH. d) Photovoltage-time spectra, e) Mott–Schottky plots at the frequency of 1000 Hz and pH 7, f) Nyquist curves, g) Bode plots, h) charge transfer rates, and i) carrier separation and injection efficiencies of the as-prepared samples. The ΔV in panel d) is the difference in voltage between dark and illumination conditions. The Nyquist curves, bode plots, and the carrier transfer efficiencies are obtained at 1.23 V vs. RHE.

electrode/electrolyte interface (Figure 4f, Figures S19–S21, and Table S4). Meanwhile, the reduced surface trapping capacitance (C_{trap}) of Sub–Bi$_2$O$_3$ at the potential range from 0.7 V to 1.23 V vs. RHE can be ascribed to the sub-O$_v$ mediated surface trap states elimination (Figure S22).[25] The density of surface states (DOS) is further derived from C_{trap} on the basis of the following relationship: $DOS = C_{trap}/q$, where q is the elementary charge quantity (1.602×10^{-19} C). DOS is inversely proportional to the photocurrent density, suggesting the direct hole transfer route on series Bi$_2$O$_3$ samples.[26] The reduced surface trap states of Sub–Bi$_2$O$_3$ within the applied potential range is benefit for surface Fermi level de-pinning and also accounts for larger V_{ph}. In the Bode plots, the obvious peak with higher phase value at low frequency region (10–30 Hz) reveals the charge transfer at electrode/electrolyte interface is the step-limiting process for PEC water oxidation (Figure 4g). The lowest phase value of Sub–Bi$_2$O$_3$ represents the trapping charge deaccumulation at the interface, consistent with the Nyquist results.[27] The photo-generated electron lifetime at the applied bias of 1.23 V can be obtained from the Bode plot according to the formula: $\tau_e = 1/(2\pi f_{min})$, where τ_e is the electron lifetime, f_{min} is the frequency at the minimum.[28] The electron lifetime of Sub–Bi$_2$O$_3$ is calculated of ~11.8 ms (Table S5), much higher than those of I–Bi$_2$O$_3$ (~6.9 ms) and P–Bi$_2$O$_3$ (~5.9 ms). The prolonged electron lifetime of Sub–Bi$_2$O$_3$ derives from the

sub-O$_v$ induced surface Fermi level de-pinning, thus promotes the photo-generated carrier transfer.

To quantify the role of Fermi level de-pinning effect on carrier transfer, the charge transfer rates (K_{ct}) were calculated by the following equation: $K_{ct} = 1/(R_{ct,trap}C_{trap})$, where the $R_{ct,trap}$ is the trapping resistance and C_{trap} is the trapping capacitance in the fitted equivalent circuit diagram, respectively (Figure 4h). The K_{ct} of Sub–Bi$_2$O$_3$ reaches ~74.8 s^{-1} at 1.23 V vs. RHE, ~4.5 and ~2.8 times larger than those of I–Bi$_2$O$_3$ and P–Bi$_2$O$_3$. Based on the accelerated charge transfer, the charge separation and injection efficiencies of Sub–Bi$_2$O$_3$ achieve 52.3 % and 92 %, respectively (Figure 4i and Figures S23–S24). Thus, photo-generated carriers can be separated efficiently to participate the PEC water splitting process.

PEC performance of the photoanodes are carried out in neutral Na$_2$SO$_4$ solution without hole scavengers (Figure 5a). The Fermi level de-pinning of Sub–Bi$_2$O$_3$ brings expanded V_{ph} and significant cathodic shift of E_{onset} (Figure S25), resulting in enhanced PEC performance. Notably, the optimal Sub–Bi$_2$O$_3$ (3.4 mA cm^{-2}) delivers ~2.3 and ~2.6 times higher photocurrent density compared to those of I–Bi$_2$O$_3$ (1.5 mA cm^{-2}) and P–Bi$_2$O$_3$ (1.3 mA cm^{-2}) photoanodes, respectively. The applied bias photo-to-current efficiency (ABPE) represents the net effect of photoelectrode by subtracting the contribution of bias potential.
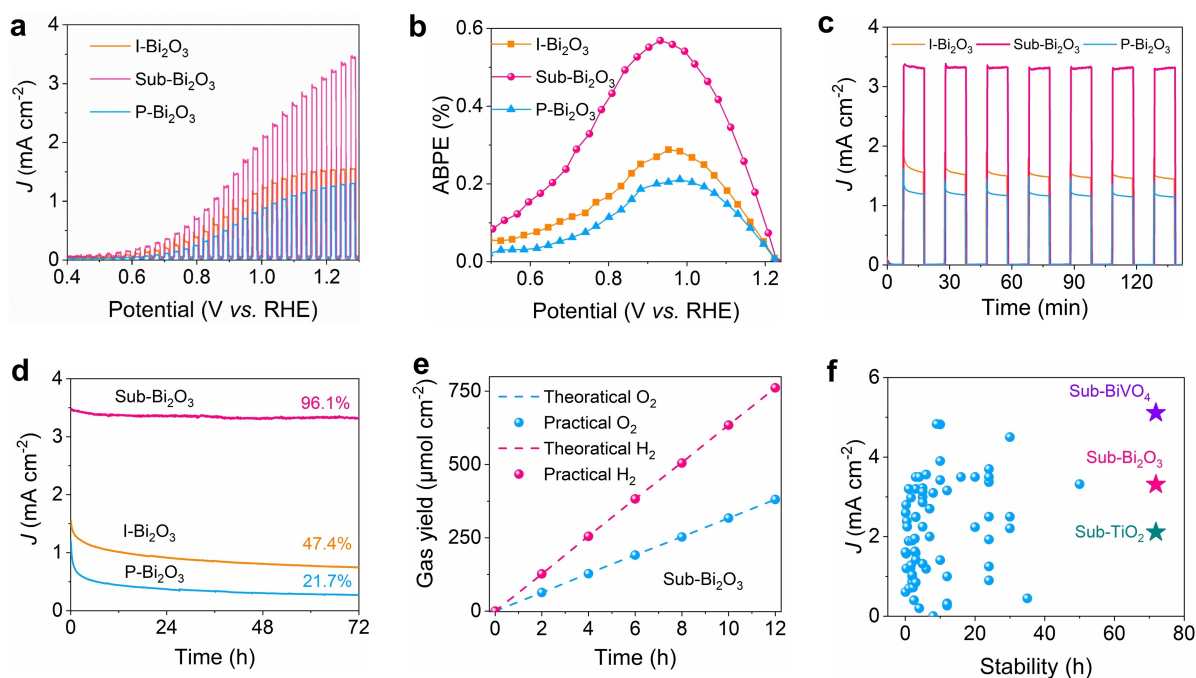
Angew. Chem. Int. Ed. **2023**, *62*, e202217026 (5 of 8)

© 2022 The Authors. Angewandte Chemie International Edition published by Wiley-VCH GmbH

Figure 5. Photoelectrochemical water splitting characterization. a) J–V plots under chopped light, b) applied bias photo-to-current efficiency, c) J–t curves under chopped light condition within 2 h, and d) steady-state photocurrent for over 72 h on as-prepared samples at 1.23 V vs. RHE under AM 1.5G simulated sunlight. e) Theoretical and practical H_2 and O_2 gas yields of Sub–Bi_2O_3. f) Summary of recent works on the photocurrent density and stability for metal oxide-based semiconductor photoanodes.

Sub–Bi_2O_3 exhibits a maximum ABPE of 0.57% at a lower potential of 0.92 V, corresponding to ~2.85 and ~2.0 times to those of I–Bi_2O_3 (0.2%) and P–Bi_2O_3 (0.28%) (Figure 5b). Compared with the I–Bi_2O_3 and P–Bi_2O_3, the applied bias potential corresponding to the ABPE maximum on Sub–Bi_2O_3 reduces by ~80 mV and ~50 mV, in line with the increased V_{ph}.[29] Meanwhile, ascribing to the Fermi level de-pinning induced promoted charge transfer, the incident photon-to-current conversion efficiency (IPCE) value of Sub–Bi_2O_3 sample reaches 50.3% at the wavelength of 375 nm, which is 1.67 and 3.2 times than that of I–Bi_2O_3 and P–Bi_2O_3 (Figure S26).

The long-term stability is then tested at 1.23 V vs. RHE under simulated sunlight. Clearly, the cliff-like photocurrent descent of I–Bi_2O_3 under chopped light condition reveals a serious carrier recombination on the photoanode surface (Figure 5c), originating from the electron capture on the intrinsic surface trap states. The PEC performance of I–Bi_2O_3 decreases sharply within the first three hours, leading to a serious attenuation to 21.7% after 72 h (Figure 5d). DFT calculations implies that the desorption of *OOH intermediate (*OOH→O_2) on I–Bi_2O_3 is the rate-limiting step with a huge overpotential of 3.8 V (Figures S27–S29). This high affinity to the oxygen intermediate and low formation energy of s-O_v lead to the instability of I–Bi_2O_3. S–O_v which easily be healed during oxygen evolution reaction (OER) process enables the rapid deterioration of the PEC performance over long-term operation condition (Figures S30–S31).[30]

By constructing sub-O_v, the Fermi level de-pinning induces efficient charge transfer, which contributes to the stable performance of Sub–Bi_2O_3 for over 72 h continued operation (remains 96.1%). On one hand, the regular and ordered outermost atomic layer (~2 nm) with no O_v acts as the self-protection layer. During the OER process, the rapid desorption of *OOH intermediate (free energy barrier of 0.3 eV for *OOH→O_2) benefits the formation of oxygen molecule and the preservation of active subsurface defective structure (Figure S27). The phase structure, morphology, and electronic structure remain intact (Figure S32), illustrative the stable characteristic of sub-O_v under operating condition. On the other hand, the rate-determining step for OER is found as the third step (*O→*OOH) with a reduced overpotential of 1.88 V, which is 0.31 V and 1.92 V lower than those of P–Bi_2O_3 (2.19 V) and I–Bi_2O_3 (3.8 V), respectively. The retained active sub-O_v structure reduces the free energy barrier of the rate-determining step, achieving robust PEC water splitting process.

Consequently, the practical gas evolution of Sub–Bi_2O_3 shows a nearly 2:1 molar ration of H_2 and O_2 generation rate, ~63.4 and ~31.7 $\mu mol\,cm^{-2}\,h^{-1}$ (Figure 5e and Figures S33–S34), which is 3 and 6 times larger than those of I–Bi_2O_3 and P–Bi_2O_3 photoanodes, respectively. The gas chromatography data of Sub–Bi_2O_3 aligns well with the theoretical yields, indicating nearly unity Faradaic efficiency.

The sub-O_v strategy is also available for other oxide semiconductors including typical $BiVO_4$ and TiO_2. Through precisely regulated sol-gel based spin coating and calcina-

tion, obvious lattice distortions are found at the sub ~2–5 nm region of Sub–BiVO$_4$ and Sub–TiO$_2$ photoanodes, ascribing to the presence of sub-O$_v$ (Figures S35–S36). Especially, the flat band potentials of Sub–BiVO$_4$ and Sub–TiO$_2$ photoanodes display a near ideal change by approximate -59 mV/pH (Figures S37–S38), illustrative the Fermi level de-pinning by the universal sub-O$_v$ strategy. Thus, the obtained Sub–BiVO$_4$ and Sub–TiO$_2$ display the outstanding photocurrent densities of ~5.1 and ~2.1 mA cm^{-2} at 1.23 V, which are ~2.7 and ~2.0 times of the pristine ones, respectively (Figures S39–S40 and Tables S6–S7). The optimal ABPE values are calculated of 0.85 % at 0.96 V on Sub–BiVO$_4$ and 0.41 % at 0.97 V on Sub-TiO$_2$ (Figures S41–S42). In addition, long-term stabilities for over 72 h are achieved in the absence of scavengers and OER cocatalysts, prominent among most reported works (Figure 5f and Table S8). Results suggest that the proposed sub-O$_v$ strategy for Fermi level de-pinning is universal and has great potential for enhancing the performance of n-type oxide semiconductors.

Conclusion

In summary, we demonstrated a general and highly effective Fermi level de-pinning strategy for robust PEC water splitting process. Through sub-O$_v$ constructing, the adverse FLP effect has been suppressed to notably boost the V_{ph} and carrier transfer. Meanwhile, the retained active sub-O$_v$ structure effectively lowers the energy barrier of the rate-determining step within OER process to improve the hysteretic water oxidation kinetics, achieving robust PEC activity in neutral electrolyte without co-catalysts and scavengers. Consequently, outstanding PEC performance on typical BiVO$_4$ (5.1 mA cm^{-2}), Bi$_2$O$_3$ (3.4 mA cm^{-2}), and TiO$_2$ (2.1 mA cm^{-2}) oxide semiconductors are achieved at 1.23 V for over 72 h, which are ~2.7, ~2.3, ~2.0 times of the pristine ones, respectively. This generic strategy paves the way to activate oxide semiconductor catalysts and extend the use of sub-O$_v$ strategy in PEC water splitting.

Conflict of Interest

The authors declare no conflict of interest.

Data Availability Statement

The data that support the findings of this study are available from the corresponding author upon reasonable request.

[1] a) Z. Wang, Y. Inoue, T. Hisatomi, R. Ishikawa, Q. Wang, T. Takata, S. Chen, N. Shibata, Y. Ikuhara, K. Domen, *Nat. Catal.* **2018**, *1*, 756–763; b) D. Lee, W. Wang, C. Zhou, X. Tong, M. Liu, G. Galli, K.-S. Choi, *Nat. Energy* **2021**, *6*, 287–294; c) X. Zhang, P. Zhai, Y. Zhang, Y. Wu, C. Wang, L. Ran, J. Gao, Z. Li, B. Zhang, Z. Fan, L. Sun, J. Hou, *J. Am. Chem. Soc.* **2021**, *143*, 20657–20669; d) C. Zhou, S. Wang, Z. Zhao, Z. Shi, S. Yan, Z. Zou, *Adv. Funct. Mater.* **2018**, *28*, 1801214.

[2] a) K. Y. Yoon, J. Park, M. Jung, S. G. Ji, H. Lee, J. H. Seo, M. J. Kwak, S. Il Seok, J. H. Lee, J. H. Jang, *Nat. Commun.* **2021**, *12*, 4309; b) S. Shoji, X. Peng, A. Yamaguchi, R. Watanabe, C. Fukuhara, Y. Cho, T. Yamamoto, S. Matsumura, M.-W. Yu, S. Ishii, T. Fujita, H. Abe, M. Miyauchi, *Nat. Catal.* **2020**, *3*, 148–153; c) Y. Chen, Y. Zhang, G. Fan, L. Song, G. Jia, H. Huang, S. Ouyang, J. Ye, Z. Li, Z. Zou, *Joule* **2021**, *5*, 3235–3251; d) L. Ran, S. Qiu, P. Zhai, Z. Li, J. Gao, X. Zhang, B. Zhang, C. Wang, L. Sun, J. Hou, *J. Am. Chem. Soc.* **2021**, *143*, 7402–7413; e) H. Zhu, Q. Yang, D. Liu, Y. Du, S. Yan, M. Gu, Z. Zou, *J. Am. Chem. Soc.* **2021**, *143*, 9236–9243.

[3] a) C. Ding, J. Shi, Z. Wang, C. Li, *ACS Catal.* **2017**, *7*, 675–688; b) C. Li, Z. Luo, T. Wang, J. Gong, *Adv. Mater.* **2018**, *30*, 1707502; c) L. Wang, Y. Lu, N. Han, C. Dong, C. Lin, S. Lu, Y. Min, K. Zhang, *Small* **2021**, *17*, 2100400; d) Y. Kuang, T. Yamada, K. Domen, *Joule* **2017**, *1*, 290–305.

[4] a) Y.-C. Ho, M. N. F. Hoque, E. Stoneham, J. Warzywoda, T. Dallas, Z. Fan, *J. Phys. Chem. C* **2017**, *121*, 23939–23946; b) M. A. Mahmud, N. K. Elumalai, M. B. Upama, D. Wang, V. R. Gonçales, M. Wright, C. Xu, F. Haque, A. Uddin, *J. Power Sources* **2018**, *383*, 59–71; c) H.-M. Li, Z.-Y. Wang, H.-J. Jing, S.-S. Yi, S.-X. Zhang, X.-Z. Yue, Z.-T. Zhang, H.-X. Lu, D.-L. Chen, *Appl. Catal. B* **2021**, *284*, 119760; d) S. C. Liu, Z. Li, Y. Yang, X. Wang, Y. X. Chen, D. J. Xue, J. S. Hu, *J. Am. Chem. Soc.* **2019**, *141*, 18075–18082.

[5] a) S. Feng, T. Wang, B. Liu, C. Hu, L. Li, Z. J. Zhao, J. Gong, *Angew. Chem. Int. Ed.* **2020**, *59*, 2044–2048; *Angew. Chem.* **2020**, *132*, 2060–2064; b) W. Wang, P. J. Strohbeen, D. Lee, C. Zhou, J. K. Kawasaki, K.-S. Choi, M. Liu, G. Galli, *Chem. Mater.* **2020**, *32*, 2899–2909; c) E. Pastor, M. Sachs, S. Selim, J. R. Durrant, A. A. Bakulin, A. Walsh, *Nat. Rev. Mater.* **2022**, *7*, 503–521.

[6] K. H. Ye, H. Li, D. Huang, S. Xiao, W. Qiu, M. Li, Y. Hu, W. Mai, H. Ji, S. Yang, *Nat. Commun.* **2019**, *10*, 3687.

[7] X. D. Wang, Y. H. Huang, J. F. Liao, Z. F. Wei, W. G. Li, Y. F. Xu, H. Y. Chen, D. B. Kuang, *Nat. Commun.* **2021**, *12*, 1202.

[8] a) L. Meng, D. Rao, W. Tian, F. Cao, X. Yan, L. Li, *Angew. Chem. Int. Ed.* **2018**, *57*, 16882–16887; *Angew. Chem.* **2018**, *130*, 17124–17129; b) S. Vanka, B. Zhou, R. A. Awni, Z. Song, F. A. Chowdhury, X. Liu, H. Hajibabaei, W. Shi, Y. Xiao, I. A. Navid, A. Pandey, R. Chen, G. A. Botton, T. W. Hamann, D. Wang, Y. Yan, Z. Mi, *ACS Energy Lett.* **2020**, *5*, 3741–3751.

[9] a) Y. C. Zhang, N. Afzal, L. Pan, X. Zhang, J. J. Zou, *Adv. Sci.* **2019**, *6*, 1900053; b) Y. Liu, Q. Zhu, X. Li, G. Zhang, Y. Liu, S. Tang, E. Sharman, J. Jiang, Y. Luo, *J. Phys. Chem. C* **2018**, *122*, 17221–17227; c) X. Sun, W. Zhu, D. Wu, C. Li, J. Wang, Y. Zhu, X. Chen, J. A. Boscoboinik, R. Sharma, G. Zhou, *Nat. Commun.* **2020**, *11*, 305.

[10] a) B. Lei, W. Cui, J. Sheng, H. Wang, P. Chen, J. Li, Y. Sun, F. Dong, *Sci. Bull.* **2020**, *65*, 467–476; b) S. Chen, H. Wang, Z. Kang, S. Jin, X. Zhang, X. Zheng, Z. Qi, J. Zhu, B. Pan, Y. Xie, *Nat. Commun.* **2019**, *10*, 788.

[11] A. Musiienko, P. Moravec, R. Grill, P. Praus, I. Vasylchenko, J. Pekarek, J. Tisdale, K. Ridzonova, E. Belas, L. Landová, B. Hu, E. Lukosi, M. Ahmadi, *Energy Environ. Sci.* **2019**, *12*, 1413–1425.

[12] M. Sun, R. T. Gao, J. He, X. Liu, T. Nakajima, X. Zhang, L. Wang, *Angew. Chem. Int. Ed.* **2021**, *60*, 17601–17607; *Angew. Chem.* **2021**, *133*, 17742–17748.

[13] a) L. Li, M. F. Lin, X. Zhang, A. Britz, A. Krishnamoorthy, R. Ma, R. K. Kalia, A. Nakano, P. Vashishta, P. Ajayan, M. C. Hoffmann, D. M. Fritz, U. Bergmann, O. V. Prezhdo, *Nano Lett.* **2019**, *19*, 6078–6086; b) Z. Chen, S. Wu, J. Ma, S. Mine, T. Toyao, M. Matsuoka, L. Wang, J. Zhang, *Angew. Chem. Int. Ed.* **2021**, *60*, 11901–11909; *Angew. Chem.* **2021**, *133*, 12008–12016.

[14] a) R. Lin, J. Wan, Y. Xiong, K. Wu, W. C. Cheong, G. Zhou, D. Wang, Q. Peng, C. Chen, Y. Li, *J. Am. Chem. Soc.* **2018**, *140*, 9078–9082; b) J. Fu, Q. Xu, J. Low, C. Jiang, J. Yu, *Appl. Catal. B* **2019**, *243*, 556–565.

[15] a) M. N. Gómez-Cerezo, M. J. Muñoz-Batista, D. Tudela, M. Fernández-García, A. Kubacka, *Appl. Catal. B* **2014**, *156–157*, 307–313; b) M. Wang, M. Shen, X. Jin, J. Tian, M. Li, Y. Zhou, L. Zhang, Y. Li, J. Shi, *ACS Catal.* **2019**, *9*, 4573–4581.

[16] a) W. Liao, H.-X. Liu, L. Qi, S. Liang, Y. Luo, F. Liu, X. Wang, C.-R. Chang, J. Zhang, L. Jiang, *Cell Rep. Phys. Sci.* **2021**, *2*, 100557; b) B. Wang, X. Wang, L. Lu, C. Zhou, Z. Xin, J. Wang, X.-k. Ke, G. Sheng, S. Yan, Z. Zou, *ACS Catal.* **2018**, *8*, 516–525.

[17] X. Peng, F. C. Zhu, Y. H. Jiang, J. J. Sun, L. P. Xiao, S. Zhou, K. C. Bustillo, L. H. Lin, J. Cheng, J. F. Li, H. G. Liao, S. G. Sun, H. Zheng, *Nat. Commun.* **2022**, *13*, 3601.

[18] a) C. Yang, X. Yu, S. Heissler, P. G. Weidler, A. Nefedov, Y. Wang, C. Woll, T. Kropp, J. Paier, J. Sauer, *Angew. Chem. Int. Ed.* **2017**, *56*, 16399–16404; *Angew. Chem.* **2017**, *129*, 16618–

16623; b) Y. Gao, R. Li, S. Chen, L. Luo, T. Cao, W. Huang, *Phys. Chem. Chem. Phys.* **2015**, *17*, 31862–31871; c) C. Sun, X. Liao, F. Xia, Y. Zhao, L. Zhang, S. Mu, S. Shi, Y. Li, H. Peng, G. Van Tendeloo, K. Zhao, J. Wu, *ACS Nano* **2020**, *14*, 6181–6190.

[19] a) M. Kim, B. Lee, H. Ju, J. Y. Kim, J. Kim, S. W. Lee, *Adv. Mater.* **2019**, *31*, 1903316; b) X. Ren, C. Wei, Y. Sun, X. Liu, F. Meng, X. Meng, S. Sun, S. Xi, Y. Du, Z. Bi, G. Shang, A. C. Fisher, L. Gu, Z. J. Xu, *Adv. Mater.* **2020**, *32*, 2001292.

[20] a) R. Simpson, R. G. White, J. F. Watts, M. A. Baker, *Appl. Surf. Sci.* **2017**, *405*, 79–87; b) J. Zemek, P. Jiricek, J. Houdkova, K. Jurek, O. Gedeon, *J. Non-Cryst. Solids* **2017**, *469*, 1–6.

[21] a) L. Xu, H. Zhao, M. Sun, B. Huang, J. Wang, J. Xia, N. Li, D. Yin, M. Luo, F. Luo, Y. Du, C. Yan, *Angew. Chem. Int. Ed.* **2019**, *58*, 11491–11496; *Angew. Chem.* **2019**, *131*, 11615–11620; b) Z. Xiao, Y. C. Huang, C. L. Dong, C. Xie, Z. Liu, S. Du, W. Chen, D. Yan, L. Tao, Z. Shu, G. Zhang, H. Duan, Y. Wang, Y. Zou, R. Chen, S. Wang, *J. Am. Chem. Soc.* **2020**, *142*, 12087–12095.

[22] A. J. Bard, A. B. Bocarsly, F. R. F. Fan, E. G. Walton, M. S. Wrighton, *J. Am. Chem. Soc.* **1980**, *102*, 3671–3677.

[23] J.-Q. Li, L. Meng, J. Cheng, *J. Phys. Chem. C* **2022**, *126*, 578–587.

[24] a) Y. C. Pu, G. Wang, K. D. Chang, Y. Ling, Y. K. Lin, B. C. Fitzmorris, C. M. Liu, X. Lu, Y. Tong, J. Z. Zhang, Y. J. Hsu, Y. Li, *Nano Lett.* **2013**, *13*, 3817–3823; b) Q. Ruan, M. K. Bayazit, V. Kiran, J. Xie, Y. Wang, J. Tang, *Chem. Commun.* **2019**, *55*, 7191–7194.

[25] B. Klahr, S. Gimenez, F. Fabregat-Santiago, T. Hamann, J. Bisquert, *J. Am. Chem. Soc.* **2012**, *134*, 4294–4302.

[26] a) H. Wang, Y. Xia, H. Li, X. Wang, Y. Yu, X. Jiao, D. Chen, *Nat. Commun.* **2020**, *11*, 3078; b) H. Zhu, M. Zhao, J. Zhou, W. Li, H. Wang, Z. Xu, L. Lu, L. Pei, Z. Shi, S. Yan, Z. Li, Z. Zou, *Appl. Catal. B* **2018**, *234*, 100–108.

[27] F. Malara, A. Minguzzi, M. Marelli, S. Morandi, R. Psaro, V. Dal Santo, A. Naldoni, *ACS Catal.* **2015**, *5*, 5292–5300.

[28] W. Li, K. Wang, X. Yang, F. Zhan, Y. Wang, M. Liu, X. Qiu, J. Li, J. Zhan, Q. Li, Y. Liu, *Chem. Eng. J.* **2020**, *379*, 122256.

[29] J. Yun, J. Tan, Y.-K. Jung, W. Yang, H. Lee, S. Ma, Y. S. Park, C. U. Lee, W. Niu, J. Lee, K. Kim, S. D. Tilley, A. Walsh, J. Moon, *ACS Energy Lett.* **2022**, *7*, 1392–1402.

[30] J. B. Pan, B. H. Wang, J. B. Wang, H. Z. Ding, W. Zhou, X. Liu, J. R. Zhang, S. Shen, J. K. Guo, L. Chen, C. T. Au, L. L. Jiang, S. F. Yin, *Angew. Chem. Int. Ed.* **2021**, *60*, 1433–1440; *Angew. Chem.* **2021**, *133*, 1453–1460.